



FINITE ELEMENT LIMIT ANALYSIS OF REINFORCED SOILS

H. S. Yu and S. W. Sloan

Department of Civil Engineering and Surveying, The University of Newcastle, N.S.W. 2308, Australia

(Received 18 July 1995)

Abstract—Finite element formulations of the lower and upper bound theorems for a reinforced soil are described. The numerical methods are based on the idea that, from a macroscopic point of view, reinforced soil can be treated as a homogeneous material with anisotropic properties. In reality, reinforced soil is a composite material whose strength relies on the interaction of the fill and the reinforcement, with the latter being comprised of metal strips or geotextile. The overall behaviour of a reinforced soil is controlled by the mechanical properties of the soil and the reinforcement, as well as their relative proportions and geometrical arrangement. Several examples are given to illustrate the effectiveness of the proposed procedures for computing rigorous bound solutions for reinforced soil structures. © 1997 Elsevier Science Ltd. All rights reserved.

INTRODUCTION

The increasing use of reinforced earth in geotechnical engineering requires the development of reliable and practical yield design methods for reinforced earth structures (Jones [1]). Although comprehensive analytical and finite element studies of reinforced soil behaviour are possible, they are inevitably complicated by the fact that the precise geometry of the reinforcement and the elastic-plastic nature of the soil needs to be fully taken into account. Examples of the analysis of reinforced soils using these types of approaches include those, among others, given by Burd [2], Rowe and Soderman [3], Abramento and Whittle [4].

The limit theorems, which have proved to be a most effective means of predicting the plastic collapse of earth structures in many areas of soil mechanics, provide an alternative approach for studying the behaviour of reinforced soil. These theorems ignore elastic deformations and are based on the assumption that, on a macroscopic scale, reinforced soil behaves as a homogeneous but anisotropic material, whose composite strength can be estimated from the strength characteristics of its components. The limit analysis procedures derived from this "homogenisation" assumption have been successfully applied to predict the observed behaviour of reinforced foundations and retaining walls in recent years (see, for example, Sawicki [5, 6] de Buhan *et al.* [7] de Buhan and Siad [8]). It is, however, often difficult to apply these analytical approaches to practical problems involving complicated loading and complex geometry.

In this paper, the limit theorems are used in conjunction with finite elements to develop a general

numerical method which can be used to compute rigorous upper and lower bound solutions for reinforced soil structures. To begin the formulation, the conventional isotropic Mohr-Coulomb yield criterion is modified to include the effect of anisotropy which is caused by the presence of reinforcement. The influence of the soil-reinforcement failure conditions on the overall behaviour is taken into account by assuming that the shear and normal stresses at the soil-reinforcement interface are governed by a general Mohr-Coulomb criterion. The numerical formulation of the lower and upper bound theorems using the modified anisotropic yield criterion is then developed. It is found that by using a suitable linear approximation of the yield surface, the application of the bound theorems leads to a linear programming problem. The solution to the lower bound linear programming problem defines a statically admissible stress field, whilst the solution to the upper bound linear programming problem defines a kinematically admissible velocity field. Since the solutions satisfy the conditions of the limit theorems precisely, the resulting collapse loads provide rigorous bounds on the true collapse load. A major advantage of using a finite element formulation of the bound theorems is that complex loading, geometry, and soil behaviour can all be dealt with easily.

FAILURE CONDITIONS FOR REINFORCED SOILS

As mentioned previously, the reinforced soil is treated as a macroscopically homogeneous but anisotropic material. The soil is assumed to be reinforced uni-directionally, which is the situation in most practical applications, and three stress tensors

are defined at every point in the homogenised continuum as shown in Fig. 1. The first tensor defines the macrostress, σ , whilst the other tensors, σ^s and σ^r , describe the microstresses which act on the soil and reinforcement respectively. In the $x - y$ plane, the reinforcement is assumed to be of thickness d and of equal normal spacing h . For the case where the proportion of the reinforcement is very small so that $d/h \ll 1$, these stresses are related (see, for example, de Buhan *et al.* [7] Sawicki [6], Sawicki and Lesniewska [9], according to

$$\sigma_x^s = \sigma_x - \sigma^r \cos^2 \theta \tag{1}$$

$$\sigma_y^s = \sigma_y - \sigma^r \sin^2 \theta \tag{2}$$

$$\tau_{xy}^s = \tau_{xy} - \sigma^r \sin \theta \cos \theta \tag{3}$$

where σ^r is the axial tensile stress acting in the reinforcement times d/h and θ represents the angle between the direction of reinforcement and the horizontal x -axis. The above equations may be derived by applying the standard stress transformation relations (Fig. 2)

$$\sigma_n = \sin^2 \theta \sigma_x + \cos^2 \theta \sigma_y - \sin 2\theta \tau_{xy} \tag{4}$$

$$\tau = -\frac{1}{2} \sin 2\theta \sigma_x + \frac{1}{2} \sin 2\theta \sigma_y + \cos 2\theta \tau_{xy} \tag{5}$$

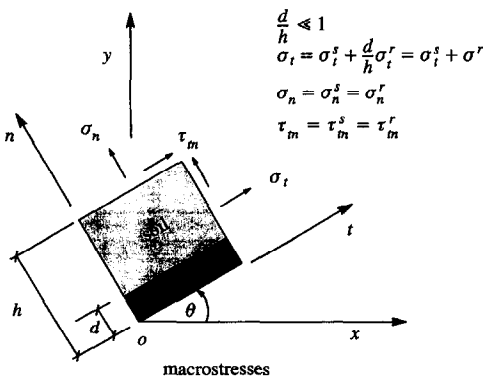
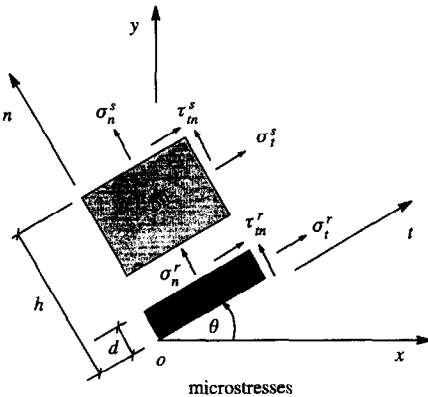


Fig. 1. Stresses on reinforced soil.

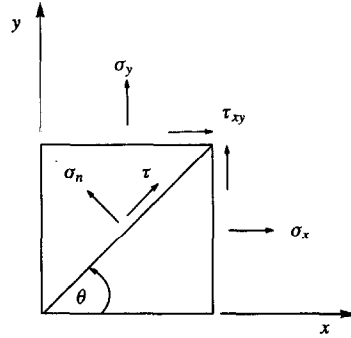


Fig. 2. Stress transformation.

to resolve the difference between the macrostresses σ and soil microstresses σ^s in the $x - y$ plane. Following de Buhan *et al.* [7], it is assumed that the reinforcing inclusions inside the soil act merely as tensile load carrying elements, and offer no resistance to shear, bending or compression. The constraint $0 \leq \sigma^r \leq \sigma_0$ is therefore imposed on σ^r , where $\sigma_0 = (d/h) \sigma_{\text{yield}}$ and σ_{yield} denotes the actual tensile yield strength of the reinforcement. If required, the formulation can be modified easily to permit the reinforcement to carry a finite load in compression.

In this paper, the soil mass is assumed to obey the Mohr-Coulomb failure condition. Assuming plane strain conditions and that tensile stresses are taken positive, the Mohr-Coulomb criterion may be expressed as

$$F_s = (\sigma_x^s - \sigma_y^s)^2 + (2\tau_{xy}^s)^2 - (2c \cos \phi - (\sigma_x^s + \sigma_y^s) \sin \phi)^2 = 0. \tag{6}$$

This can be written in terms of the macrostresses by using eqns (1)–(3) to give

$$F_s = (\sigma_x - \sigma_y - \sigma^r \cos 2\theta)^2 + (2\tau_{xy} - \sigma^r \sin 2\theta)^2 - (2c \cos \phi - (\sigma_x + \sigma_y - \sigma^r) \sin \phi)^2 = 0. \tag{7}$$

Previously, de Buhan and Siad [8] considered the influence of specific soil-reinforcement failure conditions on the macro behaviour of reinforced soil by adopting a purely cohesive or a purely frictional interface condition. This study uses a more general cohesive-frictional failure condition to describe the limiting strength of the soil-reinforcement interface according to

$$F_i = |\tau| - c_i + \sigma_n \tan \phi_i = 0 \tag{8}$$

where τ is the shear stress, σ_n is the normal stress, and c_i and ϕ_i denote the interface cohesion and interface friction angle, respectively. The above failure criterion can be expressed in terms of the macrostress

tensor using the stress transformation relations (4) and (5) to give

$$F_1 = \frac{1}{2} |\sin 2\theta(\sigma_y - \sigma_x) + 2 \cos 2\theta \tau_{xy}| - c_1 + (\sin^2 \theta \sigma_x + \cos^2 \theta \sigma_y - \sin 2\theta \tau_{xy}) \tan \phi_1 = 0. \quad (9)$$

FINITE ELEMENT FORMULATION OF THE LOWER BOUND THEOREM

Following Sloan [10], a three-noded triangular element is used in the finite element formulation of the lower bound theorem. The variation of the stresses throughout each element is assumed to be linear and, as shown in Fig. 3, each node is associated with 4 unknown stresses, σ_x , σ_y , τ_{xy} and σ^f . The stresses may be written in the form

$$\begin{aligned} \sigma_x &= \sum_{i=1}^{i=3} N_i \sigma_{xi}; & \sigma_y &= \sum_{i=1}^{i=3} N_i \sigma_{yi}; \\ \tau_{xy} &= \sum_{i=1}^{i=3} N_i \tau_{xyi}; & \sigma^f &= \sum_{i=1}^{i=3} N_i \sigma_i^f \end{aligned} \quad (10)$$

where N_i are linear shape functions and σ_{xi} , σ_{yi} , τ_{xyi} , σ_i^f are nodal stresses. Unlike the more familiar types of elements used in the displacement finite element method, each node is unique to a single element and several nodes may share the same coordinates. This feature arises because statically admissible stress discontinuities are permitted at all edges that are shared by adjacent triangles. A rigorous lower bound on the exact collapse load is ensured by insisting that the stresses obey equilibrium and satisfy both the stress boundary conditions and the yield criterion. Each of these requirements imposes a separate set of constraints on the nodal stresses.

As demonstrated by Pastor [11], additional extension elements can be developed to extend the solution over a semi-infinite domain and therefore provide a complete statically admissible stress field. The formulation of these elements is based on the same linear expansion as the 3-noded triangle.

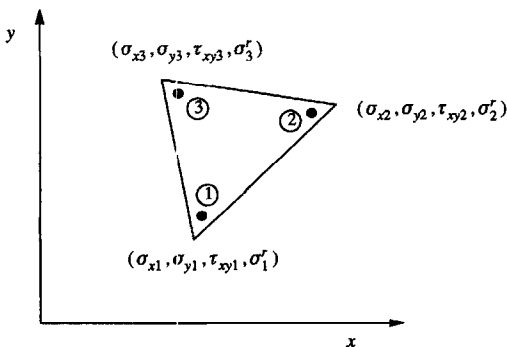


Fig. 3. Three-noded stress element for lower bound analysis.

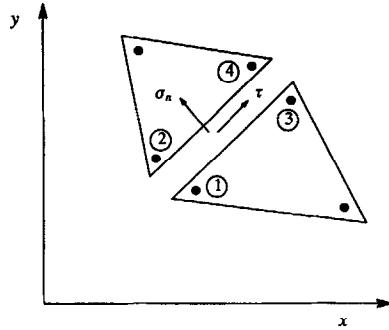


Fig. 4. Stress discontinuity.

Equilibrium

Under conditions of plane strain, the lower bound theorem insists that the stress field must satisfy the following equilibrium equations:

$$\frac{\partial \sigma_x}{\partial x} + \frac{\partial \tau_{xy}}{\partial y} = 0 \quad (11)$$

$$\frac{\partial \sigma_y}{\partial y} + \frac{\partial \tau_{xy}}{\partial x} = \gamma \quad (12)$$

where γ denotes the self-weight of the soil. Substituting eqn (10) in eqns (11) and (12) and differentiating gives two equilibrium equality constraints on the element nodal stresses:

$$\mathbf{a}_1 \mathbf{x} = \mathbf{b}_1 \quad (13)$$

where \mathbf{a}_1 is a constant matrix, $\mathbf{x} = (\sigma_{x1}, \sigma_{y1}, \tau_{xy1}, \dots, \sigma_{x3}, \sigma_{y3}, \tau_{xy3})^T$ and $\mathbf{b}_1 = (0, \gamma)^T$.

Discontinuity equilibrium

To permit statically admissible discontinuities at the edges of adjacent triangles, additional constraints on the nodal stresses need to be enforced. A statically admissible discontinuity permits the tangential stress to be discontinuous, but requires that continuity of the corresponding shear and normal stress components is retained. For the discontinuity shown in Fig. 4, application of eqns (4) and (5) at each of the nodal pairs (1, 2) and (3, 4) gives rise to four equality constraints on the nodal stresses:

$$\mathbf{a}_2 \mathbf{x} = \mathbf{b}_2 \quad (14)$$

where \mathbf{a}_2 is a constant matrix, $\mathbf{x} = (\sigma_{x1}, \sigma_{y1}, \tau_{xy1}, \dots, \sigma_{x4}, \sigma_{y4}, \tau_{xy4})^T$ and $\mathbf{b}_2 = (0, 0, 0, 0)^T$.

Stress boundary conditions

In order to satisfy the stress boundary conditions, the normal and shear stresses must be equal to their prescribed values on the boundaries of the mesh. If an edge is defined by the nodes (1, 2), and the normal

and shear stress pairs at each node are prescribed to be (q_1, t_1) and (q_2, t_2) , then substitution into the stress transformation equations leads to four equality constraints of the form:

$$\mathbf{a}_3 \mathbf{x} = \mathbf{b}_3 \tag{15}$$

where \mathbf{a}_3 denotes a constant matrix, $\mathbf{x} = (\sigma_{x1}, \sigma_{y1}, \tau_{xy1}, \sigma_{x2}, \sigma_{y2}, \tau_{xy2})$ and $\mathbf{b}_3 = (q_1, t_1, q_2, t_2)^T$.

Yield condition

As described in an earlier section, the effects of the soil reinforcement are incorporated in the analysis by modifying the yield criterion to be anisotropic. For a reinforced soil, the overall failure conditions are expressed by eqns (7) and (8). To ensure that the yield conditions are satisfied, it is necessary to impose the constraints $F_s \leq 0$ and $F_i \leq 0$. From eqn (9), it is readily seen that $F_i \leq 0$ results in two linear constraints on the stresses. Nonlinear constraints, however, will be obtained by imposing the inequality $F_s \leq 0$, since the yield function F_s is quadratic in the unknown stresses. Since we wish to formulate the lower bound theorem as a linear programming problem, it is necessary to approximate (7) by a yield criterion which is a linear function of unknown stress variables. The linearised yield surface must lie inside the modified Mohr–Coulomb yield surface in stress space so that the solution obtained is a rigorous lower bound.

With reference to Fig. 5, the linearised form of F_s can be shown to be:

$$A_k \sigma_x + B_k \sigma_y + C_k \tau_{xy} + D_k \sigma' \leq 2c \cos \phi \cos(\pi/p);$$

$$k = 1, 2, \dots, p \tag{16}$$

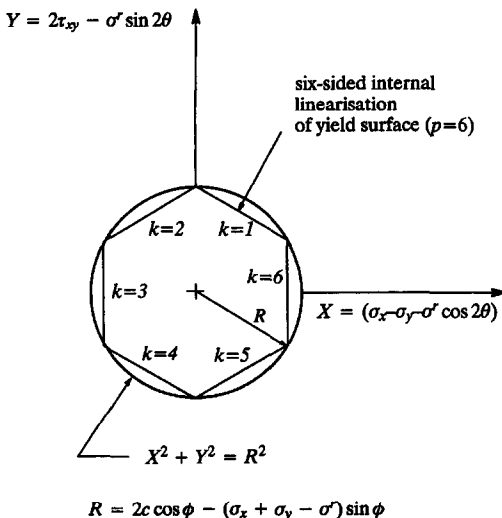


Fig. 5. Internal linearization of yield surface for lower bound analysis.

where p is the number of sides used to approximate the yield surface and

$$A_k = \cos(2\pi k/p) + \sin \phi \cos(\pi/p)$$

$$B_k = -\cos(2\pi k/p) + \sin \phi \cos(\pi/p)$$

$$C_k = 2 \sin(2\pi k/p)$$

$$D_k = -\cos 2\theta \cos(2\pi k/p) - \sin 2\theta \sin(2\pi k/p) - \sin \phi \cos(\pi/p).$$

Thus the linearised yield condition for the homogenised reinforced soil imposes p inequality constraints on the macrostresses at any given point. Similarly, the failure criterion for the soil-reinforcement interface (9) leads to two linear inequality constraints on the unknown macrostresses:

$$A_k \sigma_x + B_k \sigma_y + C_k \tau_{xy} \leq c_i; \quad k = p + 1, p + 2 \tag{17}$$

where

$$A_{p+1} = \sin^2 \theta \tan \phi_i - \frac{1}{2} \sin 2\theta$$

$$B_{p+1} = \cos^2 \theta \tan \phi_i + \frac{1}{2} \sin 2\theta$$

$$C_{p+1} = -\sin 2\theta \tan \phi_i + \cos 2\theta$$

$$A_{p+2} = \sin^2 \theta \tan \phi_i + \frac{1}{2} \sin 2\theta$$

$$B_{p+2} = \cos^2 \theta \tan \phi_i - \frac{1}{2} \sin 2\theta$$

$$C_{p+2} = -\sin 2\theta \tan \phi_i - \cos 2\theta.$$

Since the reinforcement is assumed to carry negligible load in compression and a finite load in tension, we also need to impose the additional restriction

$$0 \leq \sigma' \leq \sigma_0 \tag{18}$$

where σ_0 is the tensile yield strength of the reinforcement times the volume fraction of the reinforcement.

It is sufficient to enforce the inequalities (16)–(18) on each set of nodal stresses in order that they are satisfied throughout the mesh.

The yield conditions of (16) and (17) give rise to $p + 2$ inequality constraints on the stresses at each node i in the grid. In matrix form these constraints may be expressed as:

$$\mathbf{a}_4 \mathbf{x} \leq \mathbf{b}_4 \tag{19}$$

in which \mathbf{a}_4 depends on the coefficients A_k, B_k, C_k, D_k , $\mathbf{x} = (\sigma_{x1}, \sigma_{y1}, \tau_{xy1}, \sigma')^T$ and \mathbf{b}_4 is a function of

$2c \cos \phi \cos(\pi/p)$ for $k = 1, 2, \dots, p$ or c_i for $k = p + 1, p + 2$.

Finally, the imposition of the reinforcement yield condition (18) leads to two additional inequality constraints for each node i in the grid:

$$\mathbf{a}_5 \mathbf{x} \leq \mathbf{b}_5 \quad (20)$$

in which \mathbf{a}_5 is an identity matrix, $\mathbf{x} = (-\sigma'_r, \sigma'_r)^\top$ and $\mathbf{b}_5 = (0, \sigma_0)^\top$.

Objective function

For many plane strain geotechnical problems, we seek a statically admissible stress field which maximises an integral of the normal stress σ_n over some part of the boundary. This integral corresponds to the collapse load and is expressed in terms of the unknown nodal stresses. Since the stress distribution is linear, the integration can be performed analytically for each triangle boundary edge to give

$$Q = \frac{L}{2} (\sigma_{n1} + \sigma_{n2}) = \mathbf{c}^\top \mathbf{x} \quad (21)$$

where Q is the collapse load per unit thickness, L is the length of the boundary edge and $(\sigma_{n1}, \sigma_{n2})$ are the normal stresses at its two ends. The objective function coefficients \mathbf{c} are constants which depend on the orientation and length of each edge and \mathbf{x} is a vector of cartesian stresses for the two end nodes. For some problems, such as those that occur in slope stability analysis, we wish to optimise the unit weight directly. In these cases, γ is included as an additional variable and forms the sole term in the objective function.

Lower bound linear programming problem

Once the various constraints and objective function coefficients have been assembled using eqns (13)–(15), (19)–(21), the problem of finding a statically admissible stress field which maximises the collapse load $\mathbf{C}^\top \mathbf{X}$ may be expressed as

$$\begin{aligned} &\text{Minimise} && -\mathbf{C}^\top \mathbf{X} \\ &\text{Subject to} && \mathbf{A}_1 \mathbf{X} = \mathbf{B}_1 \\ &&& \mathbf{A}_2 \mathbf{X} \leq \mathbf{B}_2 \end{aligned} \quad (22)$$

where \mathbf{X} denotes the global vector of unknown nodal stress variables; \mathbf{A}_1 , \mathbf{B}_1 represent the coefficients due to equilibrium and stress boundary conditions; \mathbf{A}_2 , \mathbf{B}_2 are coefficients for the yield conditions; and \mathbf{C} is a vector of objective function coefficients. The details of the active set procedure which is used to solve the above linear programming problem may be found in Sloan [12]. Once the unknown stresses \mathbf{X} are found from (22), they define a statically admissible stress field and, hence, the corresponding collapse load is a rigorous lower bound on the true collapse load.

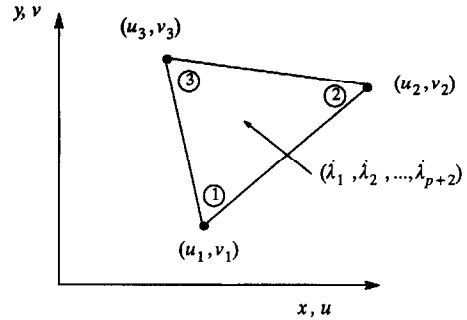


Fig. 6. Three-noded velocity element for upper bound analysis.

FINITE ELEMENT FORMULATION OF THE UPPER BOUND THEOREM

In the upper bound formulation, the tensile stress acting on the reinforcement is not treated as an unknown variable. Instead, we assume that the reinforcement will work to its maximum capacity, so that the tensile stress acting on the reinforcement is equal to the tensile strength of the reinforcement itself. This assumption is consistent with the nature of the upper bound theorem, and ensures that the resulting collapse load is a rigorous upper bound on the true solution.

Plastic flow rule

Figure 6 shows the 3-noded triangular element that is used in the finite element formulation of the upper bound theorem. Each element has 6 unknown nodal velocities and $p + 2$ plastic multiplier rates (where p is the number of sides in the linearised yield surface and each side has a plastic multiplier rate). The last two plastic multiplier rates are associated with the interface yield functions described by eqn (9). The velocities are assumed to vary linearly in each triangle according to:

$$u_i = \sum_{i=1}^3 N_i u_i; \quad v_i = \sum_{i=1}^3 N_i v_i$$

where N_i are linear shape functions and (u_i, v_i) are nodal velocities in the x - and y -directions. To ensure that the computed velocity field is kinematically admissible, the unknowns are subject to constraints which are generated by the plastic flow rule and velocity boundary conditions. To remove the stress terms from the flow rule equations, and thus provide a linear relationship between the unknown velocities and plastic multiplier rates, it is again necessary to linearise the modified Mohr–Coulomb yield criterion described by (7). To preserve the bounding property of the solution, the upper bound formulation uses an external linear approximation of the parent yield surface.

With reference to Fig. 7, the externally linearised yield function takes the following form:

$$F_k = A_k \sigma_x + B_k \sigma_y + C_k \tau_{xy} - D_k = 0; \quad k = 1, 2, \dots, p \quad (23)$$

where

$$A_k = \cos(2\pi k/p) + \sin \phi$$

$$B_k = -\cos(2\pi k/p) + \sin \phi$$

$$C_k = 2 \sin(2\pi k/p)$$

$$D_k = 2c \cos \phi + \sigma_0 [\sin \phi + \cos(2\theta - 2\pi k/p)].$$

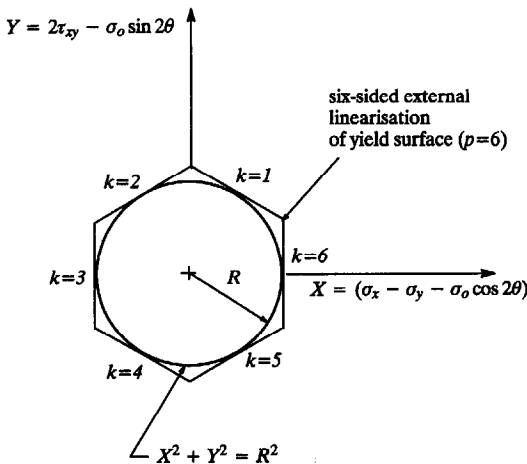
The yield function for the soil-reinforcement interface, as expressed by eqn (8), can be written in the same form as eqn (23). The values of A_k, B_k, C_k for $k = p + 1, p + 2$ are the same as those given for eqn (17) but D_k is equal to:

$$D_{p+1} = D_{p+2} = c_i.$$

For this linearised yield function, which includes the effects of the soil reinforcement and the soil-reinforcement interface, an associated flow rule gives the plastic strain rates throughout each triangular element as:

$$\dot{\epsilon}_x = \frac{\partial u}{\partial x} = \sum_{i=1}^3 \frac{\partial N_i}{\partial x} u_i = \sum_{k=1}^{p+2} \dot{\lambda}_k \frac{\partial F_k}{\partial \sigma_x} = \sum_{k=1}^{p+2} \dot{\lambda}_k A_k \quad (24)$$

$$\dot{\epsilon}_y = \frac{\partial v}{\partial y} = \sum_{i=1}^3 \frac{\partial N_i}{\partial y} v_i = \sum_{k=1}^{p+2} \dot{\lambda}_k \frac{\partial F_k}{\partial \sigma_y} = \sum_{k=1}^{p+2} \dot{\lambda}_k B_k \quad (25)$$



$$R = 2c \cos \phi - (\sigma_x + \sigma_y - \sigma_0) \sin \phi$$

Fig. 7. External linearization of yield surface for upper bound analysis.

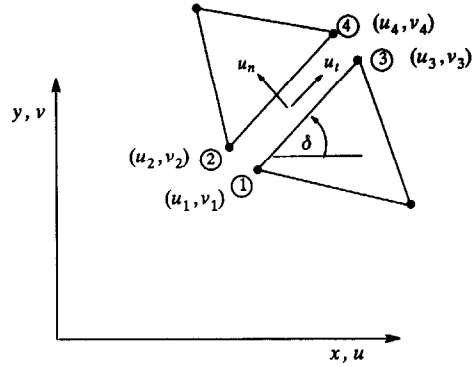


Fig. 8. Velocity discontinuity.

$$\begin{aligned} \dot{\epsilon}_{xy} &= \frac{\partial v}{\partial x} + \frac{\partial u}{\partial y} = \sum_{i=1}^3 \frac{\partial N_i}{\partial x} v_i + \sum_{i=1}^3 \frac{\partial N_i}{\partial y} u_i \\ &= \sum_{k=1}^{p+2} \dot{\lambda}_k \frac{\partial F_k}{\partial \tau_{xy}} = \sum_{k=1}^{p+2} \dot{\lambda}_k C_k \end{aligned} \quad (26)$$

where $\dot{\lambda}_k$ is the plastic multiplier rate associated with the k th side of the yield surface and $\dot{\lambda}_k \geq 0$ for $k = 1, 2, \dots, p + 2$. Since the derivatives of the linear shape functions are constant over each triangle, the flow rule of eqns (24)–(26) may be expressed as:

$$\mathbf{a}_{11} \mathbf{x}_1 + \mathbf{a}_{12} \mathbf{x}_2 = \mathbf{b}_1 \quad (27)$$

where \mathbf{a}_{11} and \mathbf{a}_{12} are matrices of constants, $\mathbf{x}_1 = (u_1, v_1, u_2, v_2, u_3, v_3)^T$, $\mathbf{b}_1 = (0, 0, 0)^T$ and $\mathbf{x}_2 = (\dot{\lambda}_1, \dot{\lambda}_2, \dots, \dot{\lambda}_{p+2})^T$.

Velocity discontinuity flow rule

In addition to general plastic deformation throughout the continuum, the upper bound formulation also permits localised plastic deformation along velocity discontinuities. A typical segment of a velocity discontinuity, inclined at an angle δ to the x -axis and defined by the nodal pairs (1, 2) and (3, 4), is shown in Fig. 8. For each discontinuity, one inequality constraint is required to ensure that the power dissipated along its length is nonnegative. The sign of each discontinuity, s , refers to the direction of the tangential velocity jump, u_t , and is defined so that $|u_t| = s u_t$ where $s = \pm 1$ and is specified as an input. Noting that the tangential velocity jump for any pair of nodes (i, j) is given by $u_t = (u_j - u_i) \cos \delta + (v_j - v_i) \sin \delta$, the sign condition $s u_t \geq 0$ gives rise to an inequality constraint of the form:

$$\mathbf{a}_2 \mathbf{x}_1 \leq \mathbf{b}_2 \quad (28)$$

where \mathbf{a}_2 is a constant matrix which depends on the discontinuity orientation and direction of slidings s , $\mathbf{x}_1 = (u_1, v_1, u_2, v_2)^T$ and $\mathbf{b}_2 = 0$. This type of constraint is enforced at each nodal pair on a velocity

discontinuity so that the sign condition is satisfied everywhere along its length.

As well as satisfying a sign condition, the discontinuity velocities must also obey the flow rule. Substituting eqns (1)–(3) in eqns (4) and (5), we see that the normal and shear microstresses for the reinforced soil are related to their macrostress counterparts according to:

$$\sigma_n^* = \sigma_n - (1 - \cos^2 \theta - \sin^2 \delta - \frac{1}{2} \sin 2\theta \sin 2\delta) \sigma_0$$

$$\tau^* = \tau - \frac{1}{2} \sin(2\theta - 2\delta) \sigma_0.$$

The Mohr–Coulomb yield criterion for a plane, which is used to describe the failure of the soil along a discontinuity, can therefore be expressed in terms of normal and shear macrostresses as follows:

$$|\tau| + \sigma_n \tan \phi = c + \sigma_0 (1 - \cos^2 \theta - \sin^2 \delta - \frac{1}{2} \sin 2\theta \sin 2\delta) \tan \phi + \frac{1}{2} \sigma_0 \sin(2\theta - \delta). \quad (29)$$

With an associated flow rule, this yield function stipulates that the normal velocity jump is related to the tangential velocity jump according to $u_n = |u_t| \tan \phi = s u_t \tan \phi$. Noting that the normal velocity jump at any pair of nodes (i, j) is given by $u_n = (u_i - u_j) \sin \delta + (v_i - v_j) \cos \delta$, this flow rule constraint may be expressed as:

$$\mathbf{a}_3 \mathbf{x}_1 = \mathbf{b}_3 \quad (30)$$

where \mathbf{a}_3 is a constant matrix which depends on the orientation of the discontinuity, $\mathbf{x}_1 = (u_1, v_1, u_2, v_2)^T$ and $\mathbf{b}_3 = 0$.

Velocity boundary condition

The boundary conditions on the velocities at node i give rise to constraints of the general form:

$$\mathbf{a}_4 \mathbf{x}_1 = \mathbf{b}_4 \quad (31)$$

where \mathbf{a}_4 is a constant matrix, $\mathbf{x}_1 = (u_i, v_i)^T$ and \mathbf{b}_4 is a vector of prescribed velocity values.

Objective function

The aim of the upper bound computation is to find a kinematically admissible velocity field which minimises the total power dissipation. To define the objective function, the dissipated power is expressed in terms of the unknown velocities and plastic multiplier rates. As the soil deforms, power dissipation may occur in the velocity discontinuities as well as in the triangles. Once the solution to the upper bound linear programming problem has been found, a rigorous upper bound on the exact collapse load is found in the usual way by equating the rate of work of the external forces to the rate of dissipation of internal energy.

For a discontinuity of unit thickness and length L , the power dissipated by sliding is given by:

$$P_d = \int_L (|\tau u_t| + \sigma_n u_n) dL$$

$$= \int_L |u_t| (|\tau| + \sigma_n \tan \phi) dL.$$

Noting that $|u_t| = s u_t$, where the sign of sliding is specified so that $s = \pm 1$, and substituting (29) we obtain

$$P_d = s [c + \sigma_0 (1 - \cos^2 \theta - \sin^2 \delta - \frac{1}{2} \sin 2\theta \sin 2\delta) \times \tan \phi + \frac{1}{2} s \sigma_0 \sin(2\theta - 2\delta)] \int_L u_t dL.$$

Since the tangential velocity jump u_t varies linearly along the discontinuity, this equation may be integrated to express P_d in the form:

$$P_d = \mathbf{c}_1^T \mathbf{x}_1 \quad (32)$$

where \mathbf{c}_1 is a vector of constants and $\mathbf{x}_1 = (u_1, v_1, u_2, v_2, u_3, v_3, u_4, v_4)^T$.

For a triangle of unit thickness and area A , the power dissipated by plastic deformation is given by:

$$P_i = \int_A (\sigma_x \dot{\epsilon}_x + \sigma_y \dot{\epsilon}_y + \tau_{xy} \dot{\gamma}_{xy}) dA.$$

Substituting the flow rule described by eqns (24)–(26), together with the linearised yield surface of (23), we see that this may be expressed as:

$$P_i = \int_A \left[\sum_{k=1}^{p+2} \hat{\lambda}_k (A_k \sigma_x + B_k \sigma_y + C_k \tau_{xy}) \right] dA$$

$$= \int_A \left[\sum_{k=1}^{p+2} \hat{\lambda}_k D_k \right] dA$$

$$= A \sum_{k=1}^{p+2} \hat{\lambda}_k D_k$$

where

$$D_k = 2c \cos \phi + \sigma_0 [\sin \phi + \cos(2\theta - 2\pi k/p)];$$

$$k = 1, 2, \dots, p$$

$$D_k = c_i; \quad k = p + 1, p + 2$$

$$\hat{\lambda}_k \geq 0; \quad k = 1, 2, \dots, p + 2.$$

This equation may also be written in the general form:

$$P_i = \mathbf{c}_2^T \mathbf{x}_2 \tag{33}$$

where \mathbf{c}_2 is a vector of constants and $\mathbf{x}_2 = (\lambda_1, \lambda_2, \dots, \lambda_{p+2})^T$.

Upper bound linear programming problem

The upper bound linear programming problem is formed by assembling the constraint coefficients from eqns (27), (28), (30) and (31), together with the objective function coefficients from (32) and (33). The task of finding a kinematically admissible velocity field, which minimises the internal power dissipation for the prescribed boundary conditions, may then be written as:

$$\begin{aligned} \text{Minimise} \quad & \mathbf{C}_1^T \mathbf{X}_1 + \mathbf{C}_2^T \mathbf{X}_2 \\ \text{Subject to} \quad & \mathbf{A}_{11} \mathbf{X}_1 + \mathbf{A}_{12} \mathbf{X}_2 = \mathbf{B}_1 \\ & \mathbf{A}_2 \mathbf{X}_1 \leq \mathbf{B}_2 \\ & \mathbf{A}_3 \mathbf{X}_1 = \mathbf{B}_3 \\ & \mathbf{A}_4 \mathbf{X}_1 = \mathbf{B}_4 \\ & \mathbf{X}_2 \geq \mathbf{0} \end{aligned}$$

where \mathbf{X}_1 is a global vector of nodal velocities and \mathbf{X}_2 is a global vector of element plastic multiplier rates. The quantity $\mathbf{C}_1^T \mathbf{X}_1$ corresponds to the total power dissipation in the velocity discontinuities which is caused by sliding, whilst $\mathbf{C}_2^T \mathbf{X}_2$ corresponds to the total power dissipation in the triangles which is caused by general plastic deformation. The nodal velocities \mathbf{X}_1 and plastic multiplier rates \mathbf{X}_2 that are found from eqn (34) define a kinematically admissible velocity field. Thus, by equating the rate of work of the external forces to the total internal power dissipation $\mathbf{C}_1^T \mathbf{X}_1 + \mathbf{C}_2^T \mathbf{X}_2$, a rigorous upper bound on the true collapse load can be found. A detailed discussion of the solution procedure for the upper bound linear programming problem may be found in Sloan [13]. A complete discussion of this aspect is not repeated here, but we note in passing that the active set algorithm of Sloan [12] is applied to the dual of eqn (34), rather than solving it directly, so that the linear programming problem can be solved efficiently.

NUMERICAL EXAMPLES

Bearing capacity of a strip footing on purely frictional reinforced soil

The first problem to be analysed, shown in Fig. 9, is the bearing capacity of a strip footing on a purely frictional soil with horizontal reinforcement. Assuming that the reinforced soil behaves as a homogeneous

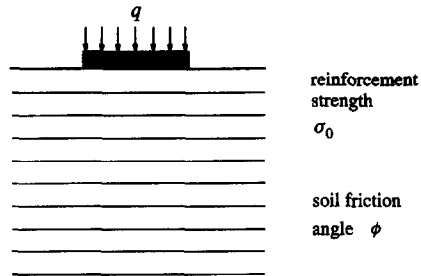


Fig. 9. Strip footing on cohesionless reinforced soil.

material with anisotropic properties, an exact bearing capacity for the case of perfectly rough soil–reinforcement interface has been obtained by Sawicki [6]. With no surcharge, the solution is as follows:

$$\frac{q}{\sigma_0} = (1 + \sin \phi) \exp \left[\left(\frac{\pi}{2} + \phi \right) \tan \phi \right].$$

The finite element meshes used for the lower and upper bound calculations are shown in Figs 10 and 11, respectively. For the case where self weight of the soil is ignored, the general solution for the bearing capacity q depends on the friction angle of the soil ϕ , the tensile strength of the reinforcement $\sigma_0 = (d/h)\sigma_{yield}$, and the roughness of the soil–reinforcement interface which is characterised by ϕ_i .

Figure 12 presents the upper and lower bounds obtained for a perfectly rough soil–reinforcement interface. These results are plotted as normalised bearing capacity against the soil friction angle. For the case of a purely frictional soil, a perfectly rough interface is one where the angle of friction on the soil–reinforcement interface is equal to the angle of friction of the soil. It is found that the upper bound solutions for the bearing capacity agree reasonably well with the lower bounds. When the soil friction

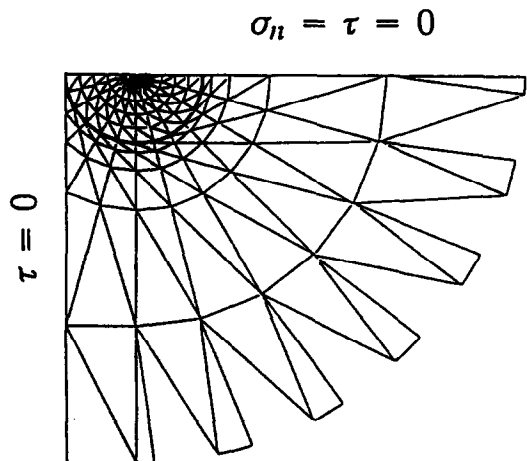


Fig. 10. Lower bound mesh for footing limit analysis.

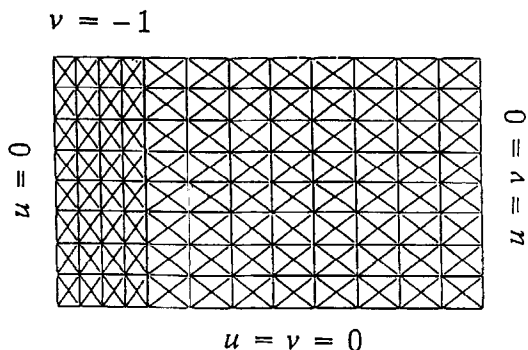


Fig. 11. Upper bound mesh used for footing limit analysis.

angle is equal to 30 degrees, the upper and lower bound solutions differ from their mean by about fifteen percent. The difference between the upper and lower bounds increases, however, with increasing friction angle of the soil. Plotted in the same figure are the upper bound solutions obtained by de Buhan and Siad [3], who also assumed a perfectly rough interface but used a rigid body mechanism to find the collapse load. The new upper bounds from the finite element formulation are clearly superior to these solutions, especially for cases where the soil friction angle exceeds about 20 degrees.

To assess the accuracy of the numerical bounding solutions, the exact result obtained by Sawicki is also plotted in Fig. 12. The exact solution lies between the numerical lower bound predictions and the numerical upper bound predictions, with the latter giving the most accurate estimate of the true collapse load. Figure 12 suggests that the exact bearing capacity solution can be predicted by the numerical upper bound analysis to within a few percent.

The effect of the soil-reinforcement interface roughness on the bearing capacity is also investigated by carrying out upper bound analyses with three different interface friction angles. The bearing capacity solutions for a perfectly smooth interface ($\phi_i = 0$), a moderately rough interface ($\phi_i = \phi/2$), and

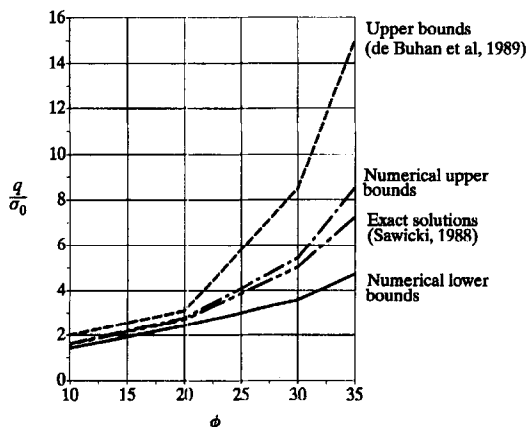


Fig. 12. Bearing capacity of strip footing on cohesionless reinforced soil with perfectly rough reinforcement.

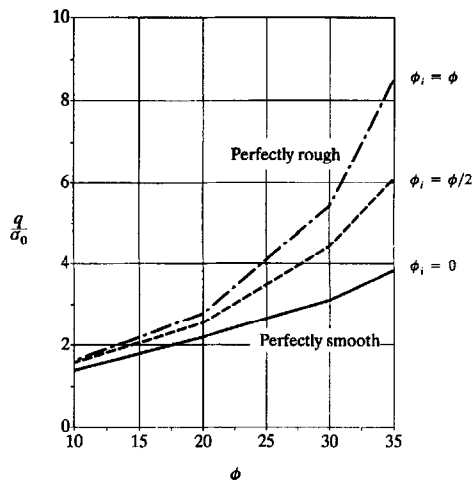


Fig. 13. Influence of reinforcement roughness on upper bound bearing capacity of strip footing on cohesionless soil.

a perfectly rough interface ($\phi_i = \phi$) are presented in Fig. 13. In agreement with de Buhan and Siad [8], it is found that the roughness of the soil reinforcement interface has a significant influence on the bearing capacity when the soil friction angle is greater than 20 degrees. Indeed, for a soil with a friction angle of 30 degrees, the bearing capacity for a perfectly rough interface is over 75% higher than that for a perfectly smooth interface.

Bearing capacity of a strip footing on cohesive-frictional reinforced soil

For cohesive-frictional soils, the benefits of having horizontal reinforcement can be assessed by comparing the bearing capacities of reinforced and unreinforced soils. Figure 14 shows how the bearing capacities for reinforced and unreinforced soils vary with a dimensionless measure of the tensile strength of the reinforcement. Results are presented for friction angles of 10, 20 and 30° and are derived from numerical upper bound computations with a perfectly rough soil-reinforcement interface. As expected, the benefit of the reinforcement increases as the strength of the reinforcement is increased. Indeed, the bearing capacity ratio $q_{reinforced}/q_{unreinforced}$ increases almost linearly with the ratio σ_0/c . It is interesting to note, however, that the benefit from horizontal reinforcement is not strongly dependent on the soil friction angle and is slightly less for soils with high friction angles.

Stability of a purely frictional reinforced wall

This section considers the stability of a vertical cut in a purely frictional reinforced soil as shown in Fig. 15. A rigorous upper bound solution to this problem has been obtained by Sawicki [6] who used a simple rigid body failure mechanism. The stability factor for the reinforced wall can be shown to be $\gamma H/\sigma_0$, where γ is the unit weight of the soil and σ_0 is a measure of the tensile strength of the reinforcement.

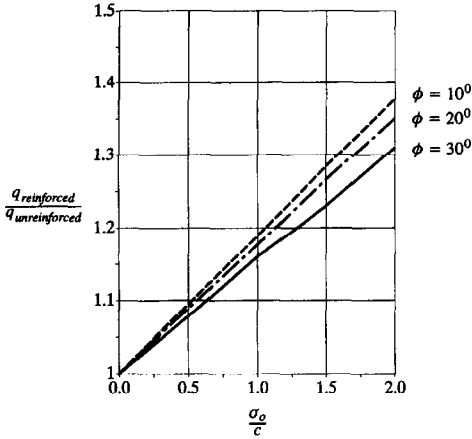


Fig. 14. Effect of reinforcement on upper bound bearing capacity for strip footing on cohesive-frictional soil.

To check the accuracy of the upper bound solution of Sawicki [6], a numerical lower bound analysis was carried out using the mesh shown in Fig. 16. The results, for the case of a perfectly rough soil-reinforcement interface, are presented in Fig. 17 where the stability factor is plotted against the soil friction angle. Shown in the same figure is Sawicki's upper bound solution. As expected, the stability factor increases as the soil friction angle increases. A comparison of the upper and lower bound solutions indicates that they bracket the exact solution quite well, with the upper bounds typically being about 20% higher than the lower bounds. Considering the difficulties in measuring soil friction angles accurately, these bounding solutions are certainly precise enough for the design of reinforced walls.

Figure 17 also indicates that the numerical lower bound solution is significantly higher than the analytical lower bound solution derived by Sawicki [6]. This suggests that the numerical lower bound formulation proposed in this paper can be used to improve existing lower bound solutions that have been derived from conventional hand calculation.

Stability of a cohesive-frictional reinforced wall

To assess the benefits of having horizontal reinforcement for cohesive-frictional walls, numerical lower bound stability analyses were performed for

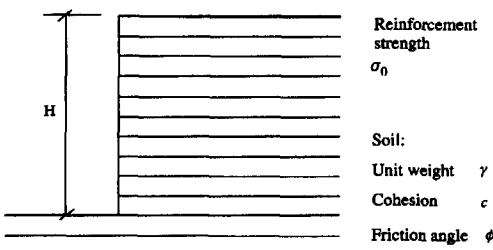


Fig. 15. Reinforced earth wall.

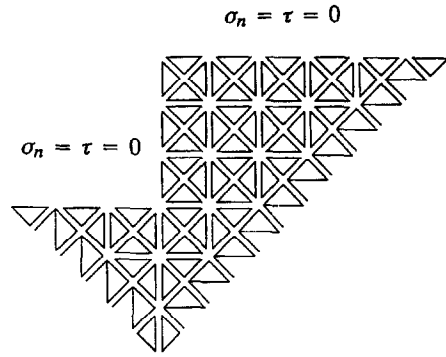


Fig. 16. Lower bound mesh used for reinforced wall limit analysis.

cases with and without reinforcement. The results are presented in Fig. 18, where the ratio of the critical heights for the two cases is plotted against a measure of the strength of the reinforcement. As we can see, the critical height ratio, $H_{reinforced}/H_{unreinforced}$, increases linearly with the measure of reinforcement strength σ_0/c .

The results for the three different friction angles shown in Fig. 18 indicate that, unlike the footing problem discussed previously, the benefits of the horizontal reinforcement actually increase quite significantly with the friction angle of the soil. For example, when the tensile strength of reinforcement is twice the soil cohesion, the ratios of the lower bound critical heights of the reinforced and unreinforced walls are 2.07, 2.37 and 2.68, respectively, for friction angles of 10, 20 and 30°.

CONCLUSION

A general finite element formulation of the lower and upper bound theorems for a reinforced soil has been developed. The numerical model assumes that the reinforced soil can be treated as a homogeneous material with anisotropic properties.

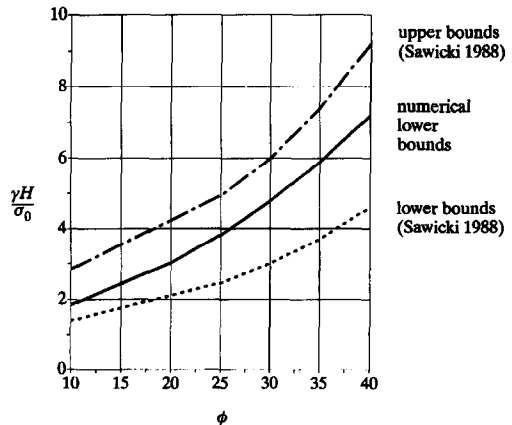


Fig. 17. Stability factor against friction angle for retaining wall in cohesionless reinforced soil.

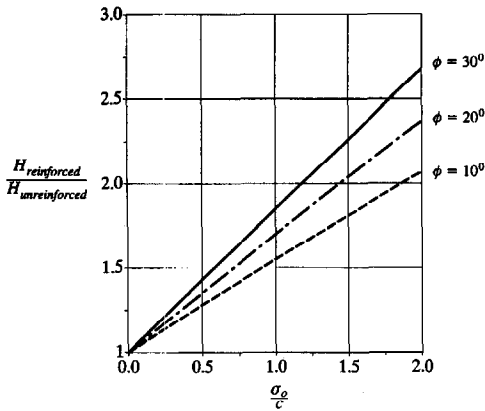


Fig. 18. Effect of reinforcement on lower bound critical height for retaining wall in cohesive-frictional soil.

The influence of the soil–reinforcement interface roughness on the overall reinforced soil behaviour has been taken into account by assuming that the shear and normal stresses on the interface are governed by a general Mohr–Coulomb criterion. The numerical examples presented in the paper suggest that the proposed numerical procedure can be successfully used for limit analysis of reinforced soil structures.

REFERENCES

1. C. J. F. P. Jones, *Earth Reinforcement and Soil Structures*. Butterworths, London, England (1988).
2. H. J. Burd, A large displacement finite element analysis of a reinforced unpaved road. PhD thesis, Oxford University, England (1986).
3. R. K. Rowe and K. L. Soderman, Stabilization of very soft soils using high strength geosynthetics: the role of finite element analyses. *Geotext. Geomem.* **6** (1) 53–80 (1987).
4. M. Abramento and A. J. Whittle, Shear-lag analysis of planar soil reinforcement in plane strain compression. *J. Engng Mech., ASCE* **119** (2) 270–291 (1993).
5. A. Sawicki, Plastic limit behaviour of reinforced earth. *J. Geotech. Engng, ASCE* **109**, 1000–1005 (1983).
6. A. Sawicki, Plastic behavior of reinforced earth. In *Civil Engineering Practice*, Vol. 3, Chap. 3, *Geotechnical Ocean Engineering*, ed. P. N. Chermisinoff, N. P. Chermisinoff and S. L. Cheng, pp. 45–64 (1988).
7. P. de Buhan, R. Mangiavacchi, R. Nova, G. Pelligrini and J. Salencon, Yield design of reinforced earth walls by a homogenization method. *Geotech.* **39**, 189–201 (1989).
8. P. de Buhan and L. Siad, Influence of a soil-strip interface failure condition on the yield strength of reinforced earth. *Comput. Geotechnics* **7**, 3–18 (1989).
9. A. Sawicki and D. Lesniewska, Limit analysis of cohesive slopes reinforced with geotextiles. *Comput. Geotechnics* **7**, 53–66 (1989).
10. S. W. Sloan, Lower bound limit analysis using finite elements and linear programming. *Int. J. Numer. Analytical Meth. Geomech.* **12**, 61–77 (1988a).
11. J. Pastor, Limit analysis: numerical determination of complete statical solutions. Application to the vertical cut. *J. Mec. Appl.* **2**, 167–198 (1978) (in French).
12. S. W. Sloan, A steepest edge active set algorithm for solving sparse linear programming problems. *Int. J. Numer. Meth. Engng* **26**, 2671–2685 (1988b).
13. S. W. Sloan, Upper bound limit analysis using finite elements and linear programming. *Int. J. Numer. Analytical Meth. Geomech.* **13**, 263–282 (1989).